Author responses to comments of Reviewer n. 1 for the manuscript "Assessing the spatial and temporal variability of methylmercury biogeochemistry and bioaccumulation in the Mediterranean Sea with a coupled 3D model"

Reviewer: A coupled transport-biogeochemical-metal bioaccumulation model is developed in this study and is applied to simulate the biogeochemical cycling of Hg in the Mediterranean Sea. The model results reveal the spatial and temporal variation of methylmercury concentrations in this region and its pattern in the plankton food webs. I find the model scheme and parameters are up to date and has several novel features that have not been considered in previous modeling efforts, which I think are important progress in this field:

1. **Online coupling with biogeochemical models facilitates the sensitivity analysis of biogeochemical parameters such as POC sinking velocity. The findings that this speed can influence the depth of maximum MeHg concentrations are interesting. This is a parameter that can be constrained by observations, pointing to important future research directions.**
2. **The inclusion of DOC-bound Hg pools, and a 4-pool partitioning scheme: POC, DOC, HgCl, and dissolved phase. Different Kd values are also used for different pools.**

In addition, the authors have a detailed analysis of the seasonal cycle of Hg cycling at different locations, well constrained by observed MeHg profiles. This highlights the importance of both hydrodynamic and biogeochemical parameters.

Here are my specific comments:

1) **Line 75: I suggest including a subsection to describe the general biogeoprovinces of the Mediterranean Sea. A very brief introduction to bathymetry and circulation patterns is also helpful. This will lay a basis for the discussion of different sites of the Sea in the later text.**

We thank the reviewer for the advice. We will add a "Study Area" section (Section 2.1) in the revised manuscript. We also have modified former Fig. 3 (Fig.1 in the revised manuscript) to show main circulation patterns. The new paragraph will read as follows:

> *The Mediterranean Sea (Fig. 1) is a semi-enclosed basin characterized by decreasing west-east gradient of primary production resulting from the superposition of biological pump and inverse estuarine circulation, as well as from the limited impact of riverine loads on the open ocean dynamics (Crise et al., 1999). Due to the formation of intermediate and deep water generating thermohaline circulation, the Mediterranean is considered a miniature of the ocean (Pinardi et al., 2019). The large-scale basin circulation (Pinardi et al., 2019, 2015, Pinardi and Masetti, 2000, and references therein) is composed of three thermohaline cells (Fig. 1). A zonal vertical circulation belt is associated with the inflow of shallow Atlantic Water (AW) at the Gibraltar Strait that becomes progressively saltier due to evaporation moving eastward (MAW, Modified Atlantic Water) and eventually sinks at intermediate depths forming the Levantine Intermediate Water (LIW), outflowing at Gibraltar. The other cells are driven by dense water formation due to winter cooling, salting, and sinking of surface water. Western Mediterranean Deep Water (WMDW) originates in the Northern Western Mediterranean Sea, while Eastern Mediterranean Deep Water (EDMW) is formed in the Adriatic Sea, but also in the Aegean and the Levantine Sea. The mixing between these deep water masses is inhibited by the shallowness of the Sicily Strait (about 500 m). Long-term observations of ocean colour (Bosc et al., 2004, Bricaud et al.,*

2002, D'Ortenzio and D'Alcalà, 2009) and coupled transport-biogeochemical models (Di Biagio et al., 2021, 2019; Lazzari et al., 2021, 2014, 2012) supported the characterization of different biogeoprovinces based on the seasonal, inter-annual, and high-frequency variability of biogeochemical processes in different areas (subbasins). Biogeochemical modelling also revealed the importance of subsurface plankton blooms, not captured by ocean colour satellite observations, highlighting the existence of a deep chlorophyll maximum that becomes deeper with increasing water oligotrophy. The most productive areas are the mesotrophic western subbasins of the Alboran Sea (Alb), Northern, and Southern Western Mediterranean (Nwm and Swm). The eastern Mediterranean is ultra-oligotrophic, apart from the Northern Adriatic Sea (Nad) which is a coastal sea, and other "intermittently blooming" areas (i.e., with high inter-annual variability) such as the Southern Adriatic Sea (Sad), the Aegean Sea (Aeg), and the

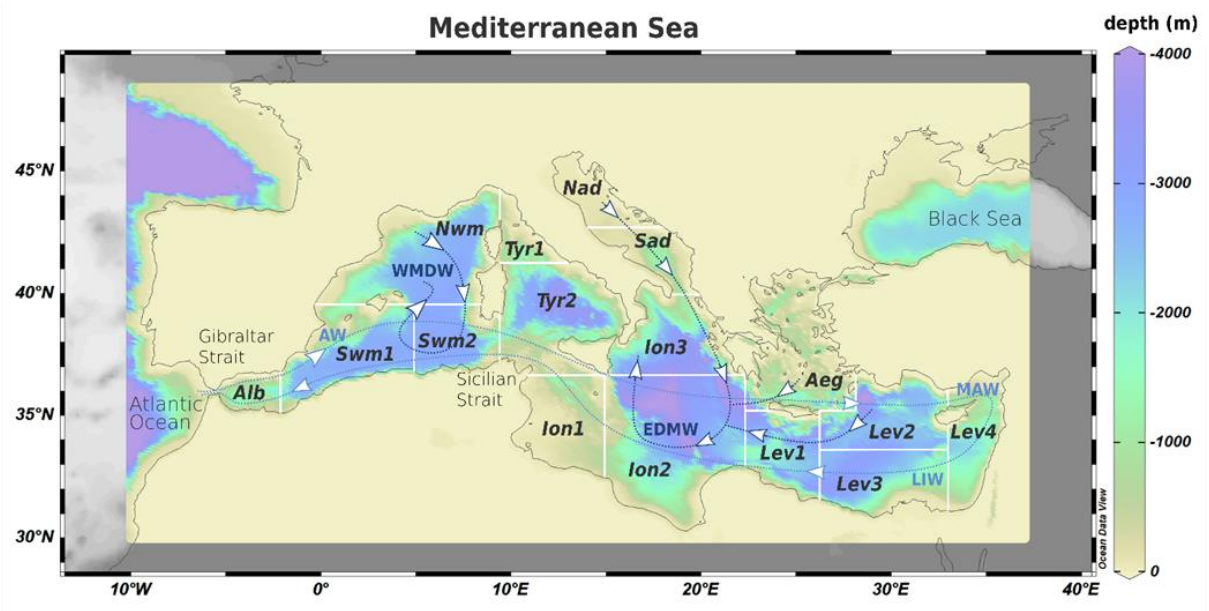

Rhodes Gyre in the Levantine Sea (Lev).

Figure 1: Bathymetric map of the Mediterranean Sea (from Ocean Data View, Schlitzer, 2014). The white contours indicate the subdivision of the model domain in subbasins: Alboran Sea (Alb), Southwest western Mediterranean (Swm1 and Swm2), Northwestern Mediterranean (Nwm), Tyrrhenian Sea (Tyr1 and Try2), northern Adriatic Sea (Nad), southern Adriatic Sea (Sad), Ionian Sea (Ion1, Ion2, and Ion3), Aegean Sea (Aeg), and Levantine basin (Lev1, Lev2, Lev3, and Lev4). The light blue line shows the zonal cell driven by the surface inflow of Atlantic Water inflow (AW) that moves eastward forming Modified Atlantic Water (MAW) and Levantine Intermediate Water (LIW), outflowing at intermediate depths at the Gibraltar Strait. The dark blue lines show the path of meridional cells related to winter convection in the Nwm, Nad, Sad, Aeg, and Lev originating the Western and Eastern Mediterranean Deep Water (WMDW and EMDW).

2) Line 105-115: need a better layout for these equations.

We agree and will adjust the equations layout as shown below:

$$\frac{d\,Hg^{II}}{dt} = -k_{met}\{Hg^{II}\} + k_{demet}\{MMHg\} - (k_{phred}+k_{biored})\{Hg^{II}_{DOC}+HgCl_n\} + (k_{phox}+k_{biox})\{Hg^{0}\} + k_{phdm}(1-\alpha)\{MMHg_{DOC}+MeHgCl\} - \omega_s\{Hg^{II}_{POC}\} \quad (1)$$

$$\frac{d\,MMHg}{dt} = +k_{met}\{Hg^{II}\} - k_{demet}\,MMHg - k_{phdm}\{MMHg_{DOC}+MMHgCl\} - k_{met}\{MMHg\} + k_{phdm2}\,DMHg - \omega_s\{MMHg_{POC}\} + Ex_{zoo}\frac{MMHg_{zoo}}{C_{zoo}} + D_{zoo}\frac{MMHg_{zoo}}{C_{zoo}} - \frac{d\,MMHg_{phy}}{dt} \quad (2)$$

$$\frac{d\,Hg^{0}}{dt} = +(k_{phred}+k_{biored})\{Hg^{II}_{DOC}+HgCl_n\} - (k_{phox}+k_{biox})\{Hg^{0}\} + \alpha k_{phdm} + \{MMHg_{DOC}+MMHgCl\} - k_{vol}\left\{Hg^{0}_{w} - \frac{Hg^{0}_{atm}}{K_{H'}}\right\} \quad (3)$$

$$\frac{dDMHg}{dt} = +k_{met}\{MMHg\} - k_{phdm2}\{DMHg\} \quad (4)$$

3) Line 114-115: This sentence is quite misleading. If the KD values reflect a balance between adsorption and remineralization, then why KD is a constant value through the whole water column, given that the remineralization rate varies drastically?

We thank the reviewer for pointing out that the sentence was unclear. We wanted to highlight that POC and DOC concentrations are dynamically simulated in space and time, affecting the value of the fractions (*$f_{Hg\text{-}POC}$, $f_{Hg\text{-}DOC}$, etc.*) and in turn the concentration of particulate Hg (cf. Eq. 5-8) even if the KD is constant along the water column. We propose rewrote the sentence as follows:

> *Field observations suggest that particulate Hg dynamics are controlled by regenerative scavenging mechanisms dependent on adsorption, remineralization, and sinking, with little influence of desorption (Lamborg et al., 2016). In the coupled OGSTM-BFM-Hg model, the dynamics POC and DOC including sinking and degradation are spatially resolved by the BFM model, and their concentrations are read by the Hg model (Figs. 2 and 3) to calculate the partitioning of HgII and MMHg […]*

4) Line 160: It's a first-order reaction approach, where does the 0.118 parameter come from? Any literature or a tunable parameter?

We clarified the paragraph as follows:

> *The bioaccumulation model simulates the MMHg uptake by the phytoplankton PFTs of the BFM model assuming that the uptake flux (Eq. (10), $nmol_{(Hg)}\ m^{-3}{}_{(w)}\ d^{-1}$) decreases at high DOC concentrations and increases with phytoplankton Surface Area:Volume ratios (R_{SV_PFT}) following the empirical relation estimated by Schartup et al., (2018) from multi-species phytoplankton uptake data (Lee et al., 2017, Lee and Fisher, 2016).*

5) Line 198: Seems that only riverine load in the dissolved phase is considered? How about riverine discharge in the particulate phase, which is the dominant form of riverine Hg discharge?

According to a recent budget estimated from Cossa et al., (2022), the magnitude of total Hg input from Mediterranean rivers is comparable to the Hg flux to the shelf sediment, suggesting that most of the Hg associated with riverine particles settles into shelf sediments, consistently with the largest Mediterranean rivers being characterized by proximal-accumulation-dominated dispersal system (Walsh and Nittrouer, 2003). Therefore, we chose as a first approximation to include only the dissolved phase, also considering that: 1) limited data are available to characterize the spatial and temporal variability of riverine Hg inputs to the Med Sea, 2) the model resolution is too coarse and limited information is available to properly address coastal processes, 3) release back to the water column by resuspension and diffusion is not simulated in this model, and 4) under the standard configuration the model did not include any source of particles from river.

We acknowledge that these methods were poorly addressed in the original manuscript, where we erroneously reported the load value for total Hg as given in Cossa et al., 2022, rather than the load used to force the model (only dissolved). We corrected the text in the revised manuscript. We also decided to run an additional simulation to explore the model response to a much higher river load of Hg, representative of both particulate and dissolved input.

We propose to add the new methods and results in the revised manuscript. The manuscript will be reorganized by adding a new subsection "Sensitivity simulation for river Hg load" to the Methods, and by adding Subsection 3.1 on Model sensitivity and uncertainty to the Results. In Subsection 3.1, we also added a comparison of modelled fluxes of Hg evasion and outflow to the Atlantic Ocean with estimates from a budget based on experimental observations following the suggestion of reviewer n. 2.

The new subsections will read as follows (Supplemental Text, Tables, and Figures are provided at the end of this document):

2.3.3 Sensitivity simulation for river Hg load

The largest Mediterranean rivers are characterized by proximal-accumulation-dominated dispersal system, i.e., deltaic systems with fast and substantial (>50-90%) sediment accumulation in the proximity of their mouth (Walsh and Nittrouer, 2003). Consistently with this picture, a recent budget for the Mediterranean Sea estimated that the magnitude of total Hg input from rivers (6 Mg y-1) is comparable to the Hg flux to the shelf sediments (6.8 Mg y-1), suggesting that most of the Hg associated with riverine particles settle before reaching the open ocean (Cossa et al., 2022). We, therefore, included only the dissolved load of Hg and MMHg in the reference simulation and explored the uncertainty related to this choice with a sensitivity simulation accounting for the total load Hg species, i.e., including both the particulate and dissolved inputs of HgII and MMHg. Limited data are available to characterize the spatial and temporal variability of these sources. The most robust observations are from a time-series (2008-2010) for the Rhône River (Cossa et al., 2017) indicating 0.85 ± 0.45 nmol g-1 of HgT and 0.017 ± 0.008 nmol g-1 of MMHg. Assessments in the Ebro River, impacted by an industrially polluted water reservoir, and in the Po River, which drain the largest Italian industrial and agricultural areas, found respectively 4.9 nmol g-1 and 1.15 nmol g-1 of particulate HgT at the river mouth, also highlighting the role of episodic stormy event in transporting large amounts of particles and associated pollutants (Palanques et al., 2020, Vignati et al., 2003). Further, at the mouth of the Soča/Isonzo River, impacted by upstream Hg mining, concentrations of unfiltered Hg higher than 200 pM have been reported (Hines et al., 2000). Hg loads for the Mediterranean tributary were estimated based on this information as synthetized in Tab. S6, also qualitatively referring to the spatial distribution of Hg stock and erosion fluxes in European topsoils (Panagos et al., 2021) and other information on

anthropogenic activities (Ahmed et al., 2018). In the reference simulation, including only the dissolved input, the loading estimate is 0.28 Mg y-1 for total dissolved Hg (and 0.008 Mg y-1 for dissolved MMHg), while in the simulation with total Hg inputs the loading is about 4.6 Mg y-1 including 0.27 Mg y-1 of MMHg. Despite the relatively high mean concentrations (Tab. S6) assumed, the estimated HgT load is slightly lower than the estimate (6 Mg y-1) from Cossa et al., (2022), most likely because the water discharge used in that work (>350 km3 y-1) is higher than the total discharge used in this model setup (>291 km3 y-1). On the other hand, the load to the Mediterranean Sea from solely European rivers (2.9 Mg y-1) estimated from Hg concentrations in topsoils and water erosion rates from river catchments (Panagos et al., 2021) is slightly lower than the load from European rivers in our model setup (3.25 Mg y-1). Finally, all these estimates are lower than the 18 Mg y-1 computed by (Liu et al., 2021) for the Mediterranean Sea through a global river model explicitly considering water discharge, suspended solids, and Hg loadings. Based on these calculations, Liu et al., (2021) proposed a global river load (1000 Mg y-1) much higher than the estimate from the latest global mercury assessment (300 Mg y-1) (UNEP, 2018). They also estimated that the 70% of the load is buried in coastal and shelf sediment.

3.1 Model sensitivity and uncertainty

The sensitivity analysis showed that the sinking rate of organic detritus (POC) is an important control on the vertical distribution of MeHg (i.e., the shape of the vertical profile) along the water column but has little effect on the values of MeHg concentrations maxima, and on the distribution of inorganic Hg species (Supplemental Sect. S1.1 and Figs. S1 and S2). On the other hand, the increase of sinking velocity from 3 to 10 m d-1 improved the agreement of modelled seasonal fluxes of POC at 200 m depth with available observations (Ramondenc et al., 2016) (Supplemental Sect. S1.1 and Fig. S3). The sensitivity also showed that the increase in the coefficient for Hg methylation (x_met) results in a best agreement with observed MeHg concentrations (Cossa et al., 2022, 2009), while the inclusion of DOC remineralization flux results in an overestimation of surficial MeHg concentrations (Supplemental Sect. S1.2 and Fig. S3).

The inclusion of higher riverine HgII, MMHg, and POC inputs does not improve the agreement between modelled and observed concentrations of MeHg (Supplemental Sect. S1.3 and Figs. S5-S10), suggesting that the underestimation of MeHg maxima in subsurface waters is not due to an underestimation of watershed sources. These results also corroborate the idea that a substantial fraction of particulate Hg and MeHg carried by rivers settles in coastal areas along with POC (Fig. S5), as estimated in a recent budget based on field observations (Cossa et al, 2022). Nonetheless, large uncertainties in the spatial and temporal variability of riverine loadings and coastal processes remain to be addressed both at the basin and global scale (Cossarini et al., 2021, Liu et al., 2021).

The underestimation of MeHg in the model does not appear to be related to inorganic Hg availability, since the concentrations of HgT are within the experimental uncertainty of the data (Fig. S11).

Modelled fluxes of HgT and Hg0 compare well with other budget estimates (Cossa et al, 2022, Žagar et al., 2007). The net exchange of Hg0 with the atmosphere indicates 44.8 Mg y-1, which is close to a previous estimate (50 Mg y-1) based on aquatic biogeochemical modelling (Žagar et al., 2007) and slightly lower than the flux adopted in the budget from Cossa and coauthors (67.5 Mg y-1). The net exchange of Hg species (~7 Mg y-1) is here significantly lower than the estimate (29.8 Mg y-1) from Cossa et al., (2020). However, while the latter estimate is based on an atmospheric model assuming a constant ocean surface Hg0 concentrations (Gencarelli et al., 2014), here, the flux is estimated accounting for 3D dynamics in the marine system, including sequestration of Hg species from surface waters due to the biological carbon pump. Recent evidence from isotopes studies pointed out that the ocean might be a net sink for atmospheric Hg, rather than a net source (Jiskra et al., 2021).

The modelled export of HgT from the Alboran Sea to the Atlantic Ocean is 9.3 Mg y-1, close to the value (9.7 Mg y-1) estimated by Cossa et al., (2022). On the other hand, our estimate (2.5 Mg y-1) of MeHg outflow is significantly lower than the 5.6 Mg y-1 of the budget by Cossa et al., (2022), even assuming an increased value for x_met and, consequently of subsurface MeHg. All in all, a calibration of the parameter x_met appears appropriate based on the current understanding, also considering that the initial guess for this parameter come from a global ocean application (Zhang et al., 2020). Indeed, such a global model study underestimated the observed MeHg concentrations in the Mediterranean Sea, while reproducing with good agreement, or overestimating, observations from various cruises in the North Atlantic and Pacific Ocean, pointing out the need to better resolve spatial and temporal variability of biological processes and linked Hg dynamics (Zhang et al., 2020). A comprehensive validation of the OGSTM-BFM biogeochemical variables (Cossarini et al., 2021) highlighted good model accuracy in surface water but higher mismatches with observed oxygen and nutrients concentrations in the mesopelagic zone, attributed to uncertainties in remineralization and deep ventilation processes, which also affect methylation dynamics. In spite of uncertainties remaining to be addressed, the OGSTM-BFM-Hg model is able to reproduce the spatial gradients observed in the Mediterranean Sea, testifying the improvements in capability to simulate Hg dynamics (Žagar et al., 2014, 2007) through the coupling with key biological processes, e.g. the carbon pump and microbial loop (Bowman et al., 2020; Cossa et al., 2017, 2009; Heimbürger et al., 2010; Monperrus et al., 2007; Munson et al., 2018; Sunderland et al., 2009).

6) **Section 2.7: It is a very meaningful practice to test the sensitivity of Hg cycling to the POC sinking velocity. Changing this parameter will not only influence Hg but also C. Are there any sediment trap observations that help to constrain the POC sinking flux itself?**

We thank the reviewer for the advice. We compared spatially and seasonally averaged model results for various subbasins with the observational dataset compiled by Ramondenc et al., (2016), choosing for each season the three subbasins having the highest number of observations. The results of this analysis, which support the choice of the settling velocity of 10 m d^{-1}.

We propose to show the results of the comparison in Fig. S3 and discuss them in the final part of Supplemental Section S1.1 (Sensitivity to POC sinking velocity) by adding the following text:

The choice to retain the simulation with w_s = 10 m d^{-1} is also supported by a comparison between the modeled POC fluxes at 200 m depth and the observational dataset compiled by Ramondenc et al., (2016). The simulation with w_s = 20 m d^{-1} was excluded a priori as it leaded to an excessive reduction of organic carbon in surface waters (Fig. S1) and did not improve model performance with regard to MeHg dynamics. The simulation with w_s = 10 m d^{-1} improved the model ability to reproduce the spring fluxes at all subbasins analyzed with respect to the simulation with w_s = 3 m d^{-1} (Fig. S3). The impact of sinking velocity on winter fluxes is very limited, while in the other seasons there are contrasting results depending on the subbasin (Fig. S3). In autumn, the agreement with observations for the simulation with w_s = 10 m d^{-1} improves for the in the Nwm and Ion subbasins but decreases for the Lev4 subbasin. Conversely, during summer, the simulation with w_s = 10 m d^{-1} leads to an overestimation of fluxes in the Nwm and Ion subbasins and to an improvement of fluxes in the Lev4.

Supplemental Material

Supplemental Section S1.3. Sensitivity to Hg river loadings

The sensitivity analysis on Hg input from rivers was performed by implementing two simulations aimed at being representative of the lower (0.28 Mg y^{-1}) and upper bound (4.6 Mg y^{-1}) of river loadings (Sect. 2.3.3 in the main text). The load of organic particles from rivers, previously not included in the model setup, was added to account for the effects of coastal sedimentation, assuming an average concentration of 5 mg l^{-1} for all the rivers (Burgeois et al., 2011). This attempt to include costal dynamics is still a first approximation for several reasons including the limited spatial and temporal coverage of data to validate coastal processes (Cossarini et al., 2021; Liu et al., 2021) and the absence in this model of a tracer for inorganic solids load.

The comparison between the modeled POC fluxes at 200 m depth and the observational dataset compiled by Ramondenc et al., (2016) performed to validate the test on sinking velocity (Supplemental Sect. 1.1) was repeated for the simulation including riverine POC sources against the refence simulation, showing very limited to no changes in the fluxes in the open waters (Fig. S5).

The results showed little sensitivity of the Hg state variables in the open waters to the prescribed variation in river loadings, as the impacts are mostly limited to coastal areas in the nearby of major rivers (Fig. S6). The highest impacts are in surface waters (0-500 m depth) (Figs. S7-S9) and variations minimum at greater depths (e.g., Fig. S10). In the western subbasins, the variation of Hg species and Hg_T concentrations in surface waters (Figure S7) is mostly in the range 1-2%, except for an increase of 3-7% in the most surficial layers (0-100 m) of the *Nwm* influenced by the high discharge of the Rhône River. In the eastern subbasins, there is more variability in response (Figs. S8-S10): the highest increases are in the coastal subbasin *Nad* (about 20% for Hg_T and >25% for MMHg) that receive high Hg loadings from the Po and Soca/Isonzo Rivers, also affecting the southernmost confining subbasin *Sad* (with variation of 10-20% for Hg_T and about 10% for MMHg in the upper 100 m). The easternmost and shallowest part of the Levantine Sea (*Lev4)* also shows relatively high variations (4-7% for Hg_T and MMHg in the first 100 m), while the impacts are lower (1-4%) in the other subbasins. Overall, these results imply small variation in modelled concentrations, and it should be noted that excluding the shallow *Nad* subbasins, the variations in MMHg concentrations are maxima at the top of the water column where concentrations are very low (<0.02-0.06 pM).

Figure S3. Seasonal dynamics of Particulate Organic Carbon fluxes in various subbasins of the Mediterranean Sea. The fluxes calculated from monthly mean model output are shown for the two simulations (Supplemental Sect. S1.1) assuming w_s = 3 m d^{-1} (dashed blue line for the average and shaded area for minimum and maximum values) and w_s =10 m d^{-1} (solid black line and grey shaded area), compared with observations (red dots and bars indicate the seasonal median and the I and III quartiles) compiled by Ramondenc et al., (2016).

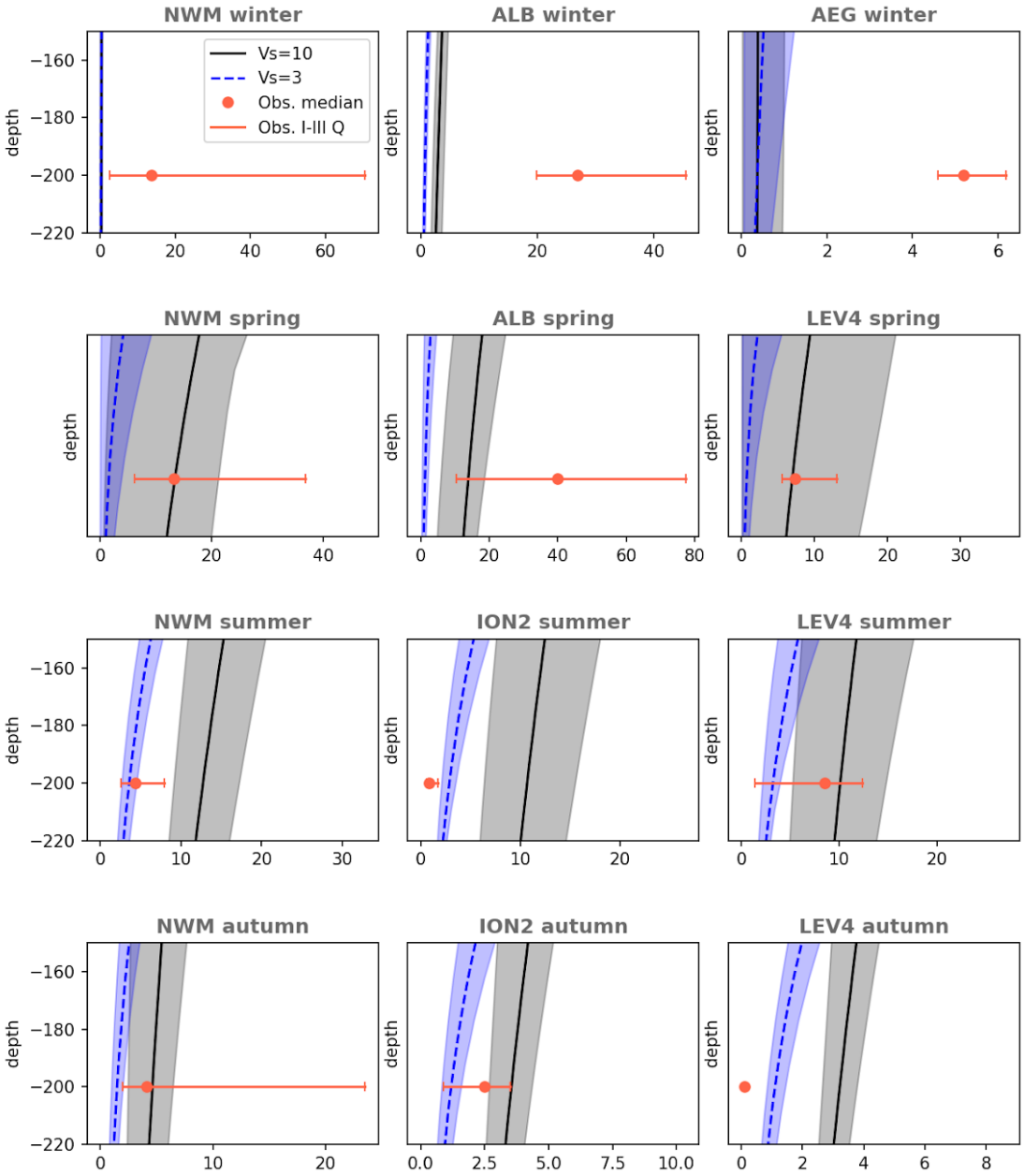

Figure S5. Seasonal dynamics of Particulate Organic Carbon fluxes in various subbasins of the Mediterranean Sea. The fluxes calculated from monthly mean model output are shown for the simulation with POC input from rivers (dashed blue line for the average and shaded area for minimum and maximum values) and for the reference simulation including only dissolved river inputs (solid black line and grey shaded area) (Supplemental Sect. S1.3), compared with observations (red dots and bars indicate the seasonal median and the I and III quartiles) compiled by Ramondenc et al., (2016).

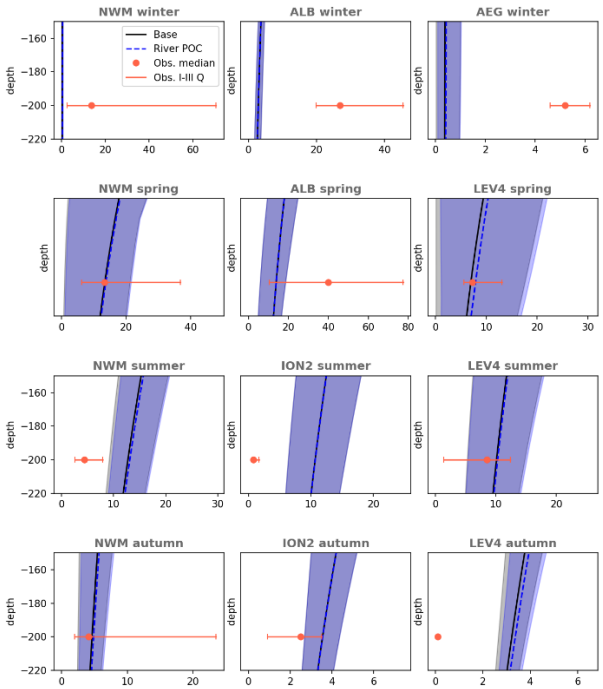

Figure S6. Spatial distribution of the variation (%) in modelled concentration of Hg^{II} for the simulation including input of particulate Hg from river (Supplemental Sect. S1.3) at different depths (25 m, 60 m, and 100 m) and months (January, April, July, and October).

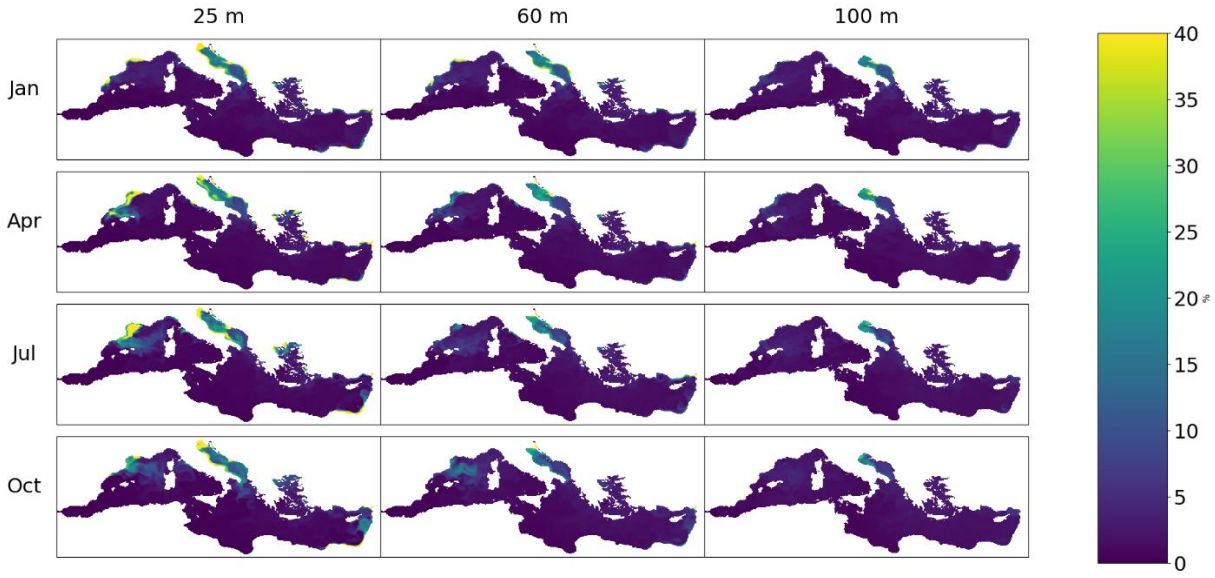

Figure S7. Impact of the simulation with high riverine Hg loads (Supplemental Sect. S1.3) on the seasonal average concentration profiles in surface waters (0-500 m depth) of different subbasins of the Western Mediterranean Sea (*Alb, Nwm, Swm, and Tyr*). The % variation with respect to the reference simulation is shown for each Hg species (Hg^{II}: yellow dashed line, Hg^{0}: dotted cyan line, MMHg: dash-dotted purple line, DMHg: dotted violet line).

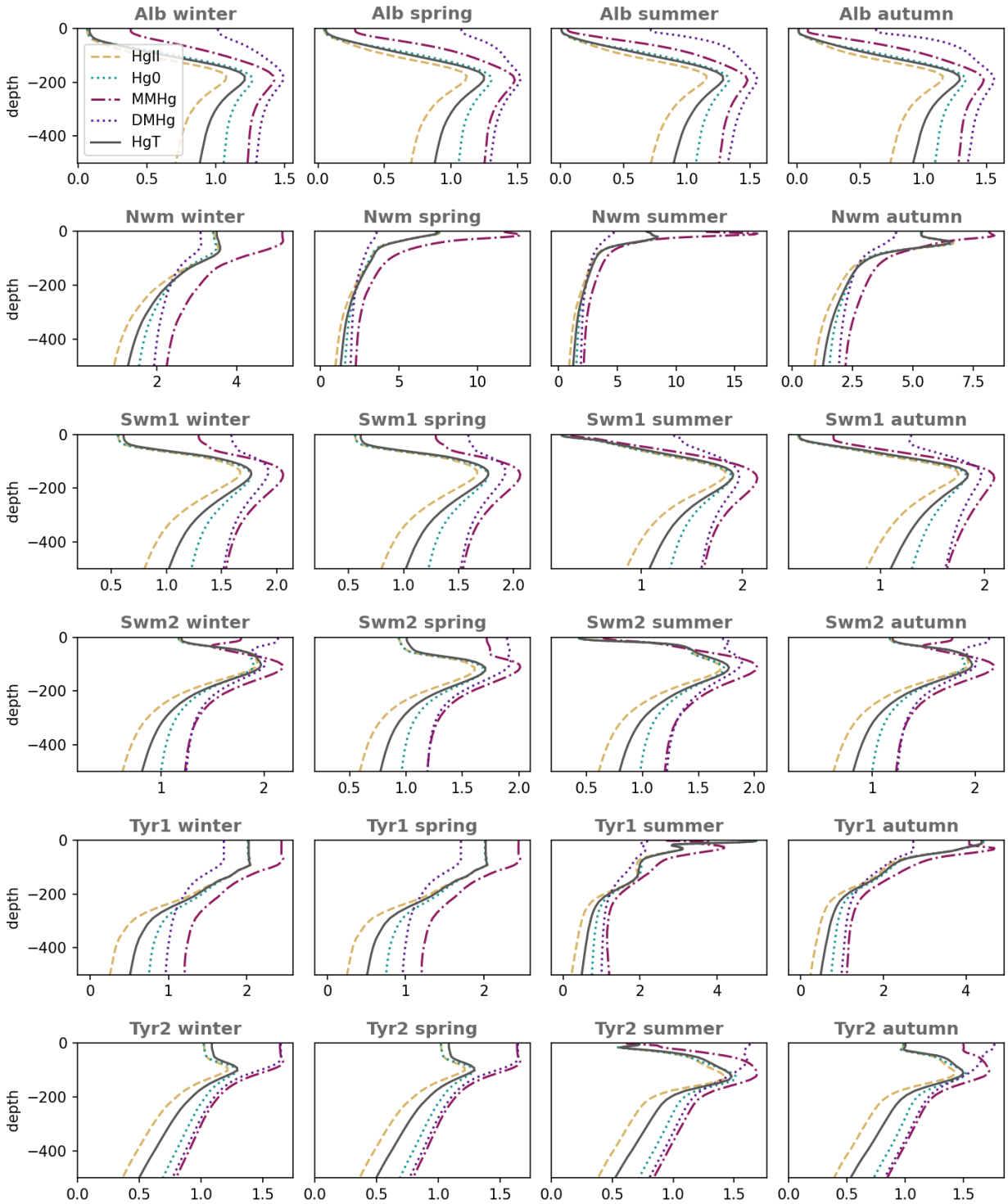

Figure S8. Impact of the simulation with high riverine Hg loads (Supplemental Sect. S1.3) on the seasonal average concentration profiles in surface waters (0-500 m depth) of different subbasins of the Eastern Mediterranean Sea (*Nad, Sad, Aeg, and Lev*). The % variation with respect to the reference simulation is shown for each Hg species (Hg^{II}: yellow dashed line, Hg^{0}: dotted cyan line, MMHg: dash-dotted purple line, DMHg: dotted violet line).

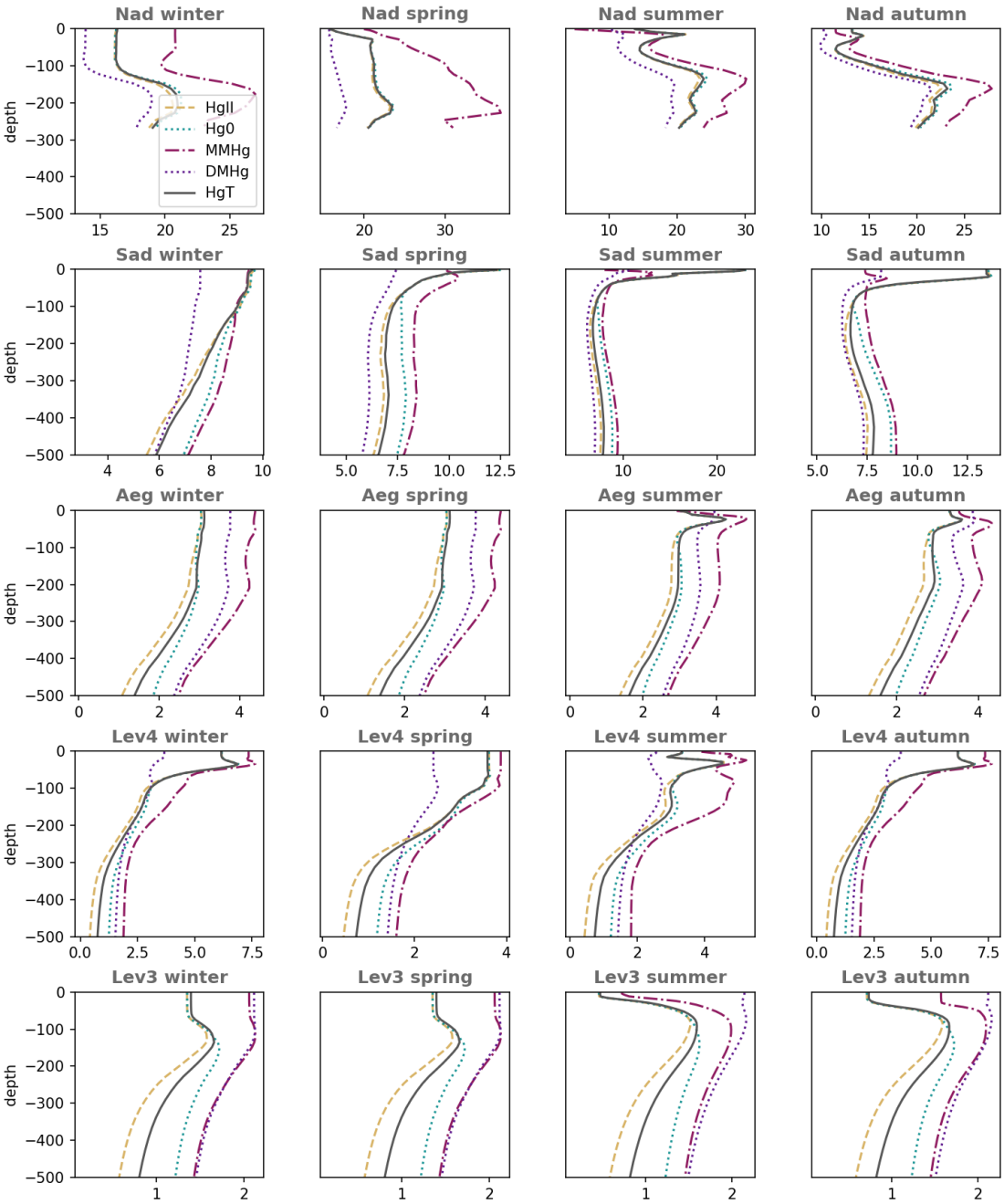

Figure S9. Impact of the simulation with high riverine Hg loads (Supplemental Sect. S1.3) on the seasonal average concentration profiles in surface waters (0-500 m depth) of different subbasins of the Eastern Mediterranean Sea (*Ion and Lev*). The % variation with respect to the reference simulation is shown for each Hg species (Hg^{II}: yellow dashed line, Hg^{0}: dotted cyan line, MMHg: dash-dotted purple line, DMHg: dotted violet line).

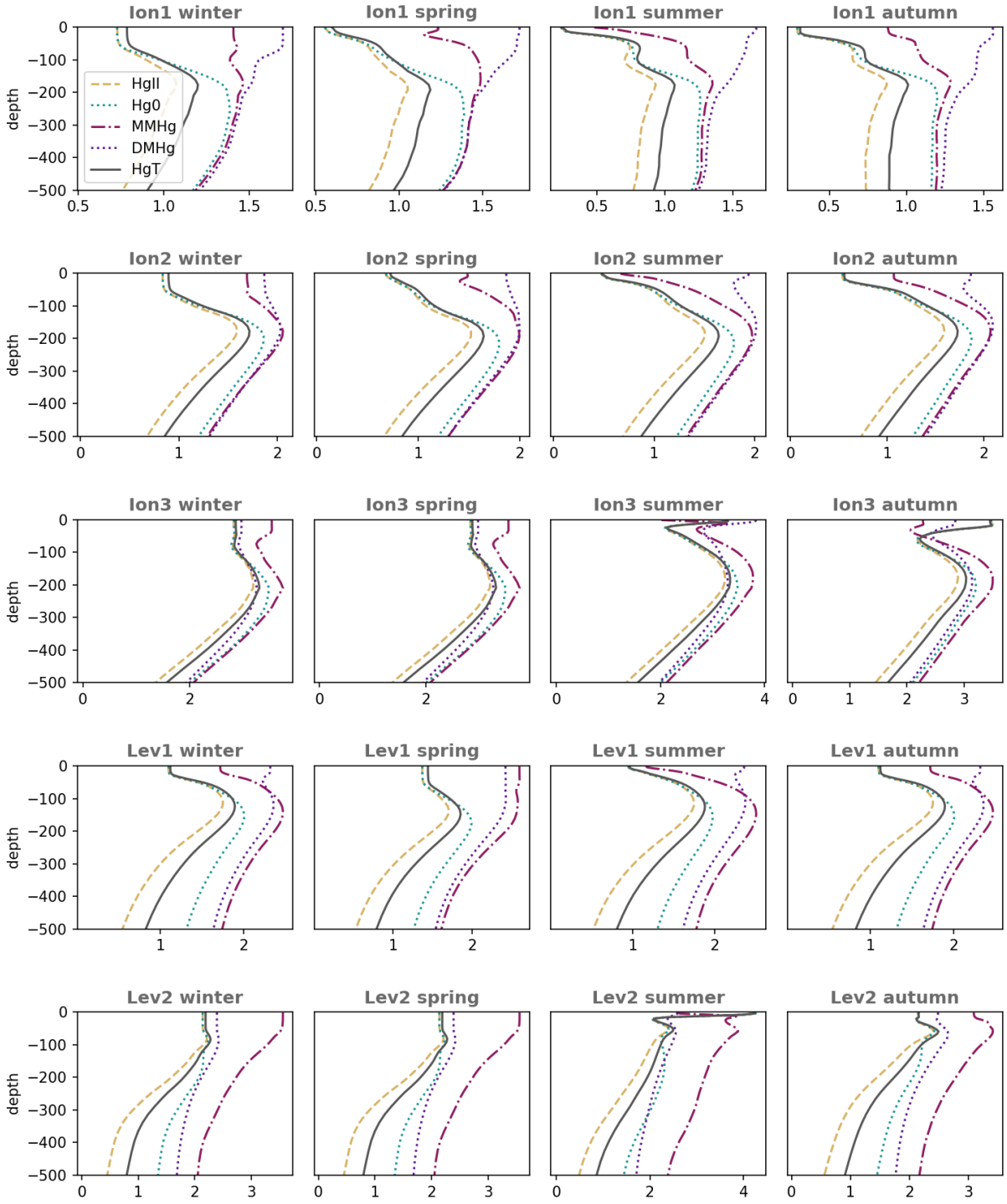

Figure S10. Impact of the simulation with high riverine Hg loads (Supplemental Sect. S1.3) on the seasonal average concentration profiles in the water column of different subbasins of the Eastern Mediterranean Sea (*Ion and Lev*). The % variation with respect to the reference simulation is shown for each Hg species (Hg^{II}: yellow dashed line, Hg^{0}: dotted cyan line, MMHg: dash-dotted purple line, DMHg: dotted violet line).

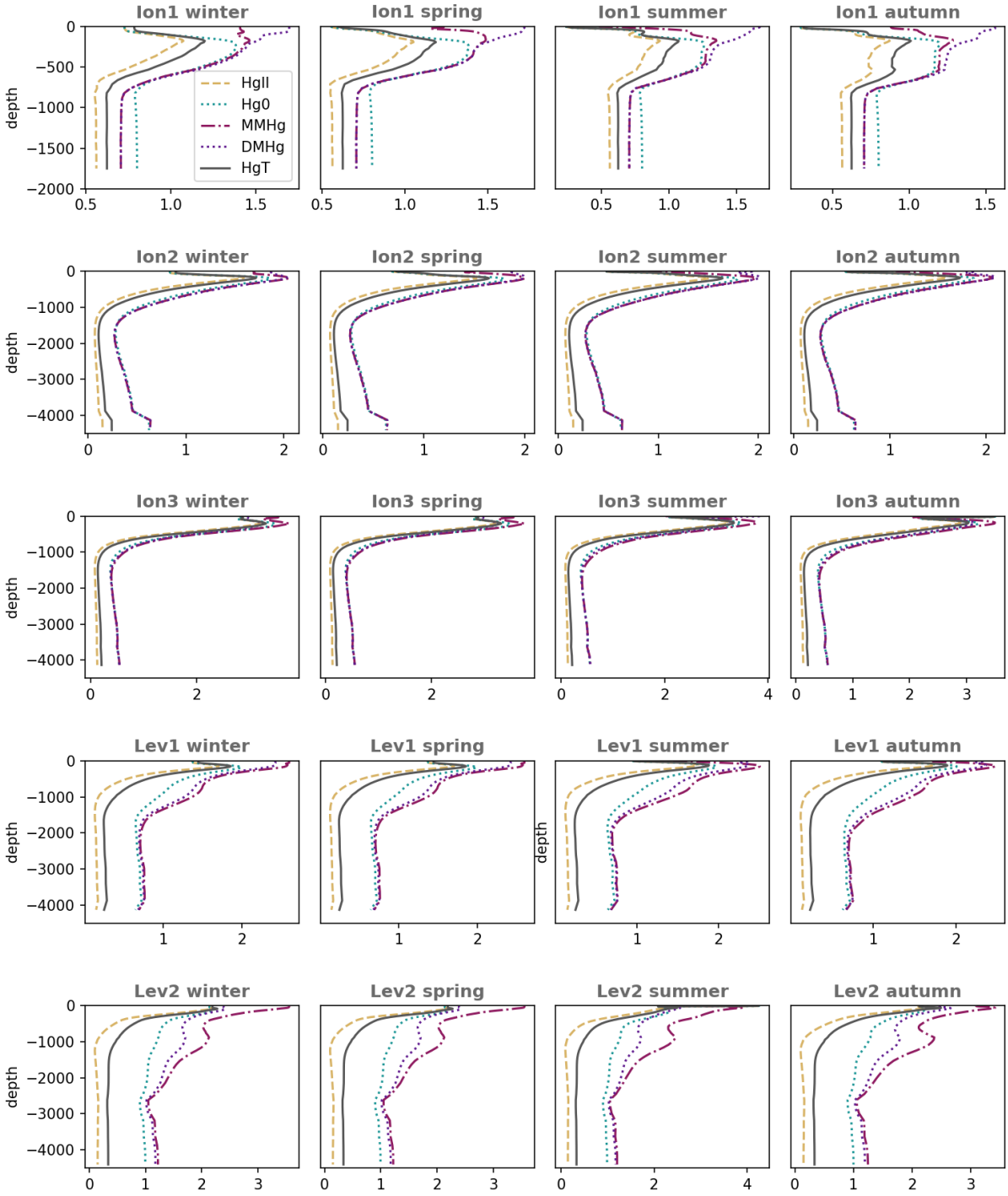

Table S6. Concentrations of riverine HgT and MMHg used in the model setup, and resulting annual load

River Name	Hg_T	MMHg	Hg_T	MMHg	Notes and References
	pM	pM	Mg y^{-1}	Mg y^{-1}	
Grand Rhone	53	1.06	0.62	0.0355	*HgP = 0.85 nmol/g* [1] *SPM = 60 mg/l* [2]
Petit Rhone	53	1.06	0.07	0.0039	
Soca/sonzo	170	1.02	0.23	0.0294	*90-249 pM at the river mouth* [3]
Ebro	102	2.04	0.23	0.0070	*HgP = 4.98 nmol/g* [4] *SPM = 20 mg/l* [4]
Po Maistra	120	2.4	0.06	0.0030	*HgP = 1.15 nmol/g* [5] *SPM = 30 mg/l* [5]
Po Tramontana	120	2.4	0.14	0.0071	
Po Dritta	120	2.4	0.39	0.0201	
Po Scirocco + Po Bonifazi	120	2.4	0.12	0.0062	
Po Bastimento	120	2.4	0.05	0.0028	
Po Bocca Tolle	120	2.4	0.20	0.0102	
Po Gnocca	120	2.4	0.21	0.0106	
Po Goro	120	2.4	0.13	0.0067	
Po Levante	120	2.4	0.02	0.0010	
Po Volano	120	2.4	0.01	0.0003	
Nile	120	2.4	0.28	0.0074	*Impacted by Artisanal Small-Scale Gold Mining* [6]
Nile	120	2.4	0.28	0.0074	
Tevere/Tiber	100	2	0.07	0.0136	*High mineral Hg content in soils* [7]
Tevere/Tiber	100	2	0.07	0.0136	
Reno	80	1.6	0.03	0.0012	*Impacted by Industries and Agriculture* [7]
Vjiose	53	1.06	0.04	0.0026	
Seman	53	1.06	0.02	0.0012	
Buna/Bojana	53	1.06	0.10	0.0060	
Buna/Bojana	53	1.06	0.10	0.0060	
Piave	53	1.06	0.05	0.0030	
Tagliamento	53	1.06	0.03	0.0018	
Livenza	53	1.06	0.04	0.0023	
Brenta-Bacchiglione	53	1.06	0.07	0.0038	
Adige	53	1.06	0.08	0.0049	
Lika	53	1.06	0.02	0.0014	
Krka	53	1.06	0.02	0.0010	
Arno	53	1.06	0.03	0.0017	

Neretva	53	1.06	0.07	0.0043
Aude	53	1.06	0.03	0.0015
Trebisjnica	53	1.06	0.03	0.0017
Mati	53	1.06	0.03	0.0018
Volturno	53	1.06	0.02	0.0009
Shkumbini	53	1.06	0.02	0.0010
Struma/Strymonas	53	1.06	0.02	0.0014
Meric/Evros/Maritsa	53	1.06	0.05	0.0028
Axios/Vardar	53	1.06	0.03	0.0016
Arachtos	53	1.06	0.02	0.0014
Pinios	53	1.06	0.02	0.0011
Acheloos	53	1.06	0.03	0.0019
Gediz	53	1.06	0.02	0.0012
Buyuk Menderes	53	1.06	0.04	0.0024
Kopru	53	1.06	0.04	0.0022
Manavagat	53	1.06	0.06	0.0032
Seyhan	53	1.06	0.07	0.0038
Ceyhan	53	1.06	0.07	0.0042
Goksu	53	1.06	0.09	0.0051
Medjerda	53	1.06	0.03	0.0017
Asi/Orontes	53	1.06	0.03	0.0015
Total Load (Mg y^{-1})			4.62	0.27

(1) Cossa et al., 2017; (2) Bourgeois et al., 2011; (3) Hines et al., 2000; (4) Palanques et al., 2020; (5) Vignati et al., 2003; (6) Ahmed et al., 2018; (7) Panagos et al., 2021